

Plasmonic Nanosensor Based on Mie Scattering in Multi-mode Metallic Nanoparticles

jun zhu (✉ zhujun1985@gxnu.edu.cn)

Guangxi Normal University <https://orcid.org/0000-0003-0461-212X>

Yihong Ren

Guangxi Normal University

Research Article

Keywords: Refractive index sensor, Mie scattering, metallic nanoparticles, Multi-mode

Posted Date: May 19th, 2021

DOI: <https://doi.org/10.21203/rs.3.rs-507563/v1>

License:   This work is licensed under a Creative Commons Attribution 4.0 International License.

[Read Full License](#)

Plasmonic nanosensor based on Mie scattering in Multi-mode Metallic Nanoparticles

JUN ZHU*¹, YIHONG REN¹

¹ College of Electronic Engineering, Guangxi Normal University, Guilin 541004, China

* zhujun1985@gxnu.edu.cn

Abstract: The scattering and absorption characteristics of light by spherical particles are often analysed based on the classical Mie scattering theory. In this paper, we study refractive index sensor of multi-mode based on the Mie scattering and its extension theories. Based on the Mie scattering theory, the light extinction, scattering, absorption cross-section, and absorption efficiency associated with the spherical particle can be calculated. The structure that we design has a long wavelength possesses a higher power than that with a short wavelength. Also, the structural parameters induces a red-shift in the resonance spectrum. Lastly, the results of multi-mode are obtained: the transmittance of modes 1, 2, and 3 vary within the ranges 0.43–0.67, 0.61–0.46, and 0.26–0.5, respectively; the figures of merit of modes 1, 2, and 3 can reach as high as 12, 27.7, and 3.8, respectively; the refractive index sensitivity can reach as high as 500 and 1000 nm/RIU. As indicated by these findings, the proposed structure can significantly improve the transmission characteristics of nanodevices. Such a structure holds significant potential for application in the field of on-chip plasma sensing and optical communication.

Keywords: Refractive index sensor ; Mie scattering ; metallic nanoparticles; Multi-mode

1. Introduction

Plasmonic nanostructures, unlike traditional optical devices, are capable of supporting electromagnetic waves at the nanoscale through the formation of surface plasmon polaritons (SPPs). Such a feature enables plasmonic nanostructures to be widely used in the design and improvement of wavelength-tunable optical devices and high-sensitivity sensors [1-6]. Among the various types of SPP waveguides, the metal-insulator-metal (MIM) plasmonic waveguide has attracted significant attention owing to its low bending loss, simple manufacturing process, flexible on-chip integration, and capability of forming strong localised surface plasmon resonance (SPR) [7-11]. In addition, MIM waveguides can confine light in the nanometre regime with an acceptable SPP propagation length. Therefore, MIM waveguides have been widely used in the inspection and detection of the refractive indices of a wide variety of materials [12-17].

In an SPP sensor, certain resonance modes are primarily excited in the straight waveguide coupled with the resonance cavity under specific conditions. These resonance conditions are considerably sensitive to the variation in the refractive index in the waveguide and the resonator geometry. In recent years, several different modes of plasmonic filters or sensors based on MIM waveguides, such as nanodiscs, nanorods, stubs, and ring-shaped resonators, have been proposed [18-19]. These innovations have resolved the challenge of the complex manufacturing process associated with the Bragg reflector and, furthermore, have provided an improved SPP propagation length along the plasmonic MIM waveguide. The structural configuration of the resonator plays a vital role in determining the resonant modes in the plasmonic MIM waveguides [20-21]. By modifying the resonator size, past researchers have developed highly sensitive nanodevices at the cost of increased complexity. For example, Qi et al. designed and analysed a plasmonic filter comprising two slot resonators and a nanodisc cavity. The sensitivity of this structure could be as high as 750 nm/RIU [22]. Guo et al. designed a refractive index sensor based on a subwavelength MIM waveguide coupled with tangent-ring resonators. The sensitivity of this sensor was as high as 880 nm/RIU [23]. The research team led by Prof. Monfared from Dalhousie University in Canada and the team led by Dr Kishore from the National Institute of Technology in India together proposed a label-free refractive index sensor based on the hybrid plasmonic resonator. By placing different analytes at the centre of the hybrid plasmonic ring, the sensitivity of the proposed refractive index sensor was evaluated to be 847.50 nm/RIU [24]. The sensitivity and figure of merit (FOM) are the two most significant

parameters to be considered when designing a sensor. A considerable amount of effort has been dedicated to the improvement of sensitivity by past researchers. However, it is still challenging to investigate the effect of resonator defects on the sensitivity and FOM improvement while maintaining the sensor size constant. Furthermore, the method of coupling is also a significant factor that affects the sensitivity.

In this study, the structure of the MIM waveguide comprising metal nanoparticles coupled with the rectangular split-ring resonator was investigated. In the proposed structure, the SPR was induced from a gold nanoparticle array coupled with the MIM waveguide. The transmission characteristics and electromagnetic field distribution characteristics of the MIM waveguide were simulated and calculated systematically for different internal parameters of the rectangular split-ring resonator and various waveguide gap widths. Finally, we calculated the refractive index sensitivity. The results indicated that the proposed structure could overcome the issue of an insufficient refractive index in conventional sensors, offering a potential application as a nanophotonic device in highly integrated optical circuits.

2 Mie scattering theory at metallic nanoparticle surface

2.1 Single-layer spherical particle

The optical properties of metallic nanoparticles can be simulated quantitatively using the light scattering theory and the size correction model for a metal dielectric function. For metallic nanoparticles with a regular shape, such as spheres and ellipsoids, the optical properties can be analysed using the analytical method of light scattering, that is, the Mie scattering theory and its extension theories [25]. The Mie scattering theory has received significant attention since its proposition and remains one of the most fundamental methods used for studying the optical properties of nanoparticles. The detailed description and derivation of the Mie scattering theory have been presented in a number of monographs on the topic of light scattering by particles [26]. The scattering and absorption characteristics of light by spherical particles are often analysed based on the classical Mie scattering theory, wherein the mutual interaction between the light and the spherical particle is illustrated in Fig. 1. As depicted in the Fig., λ denotes the wavelength of the incident light, R denotes the particle radius, n_p is the refractive index of the particle, and n_m is the refractive index of the surrounding medium. The light extinction, scattering, absorption cross-section, and absorption efficiency associated with the spherical particle can be calculated using the equations presented in the following section.

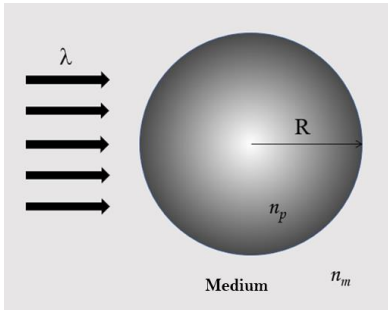


Fig. 1. Schematic of mutual interaction between incident light and single-layer spherical article

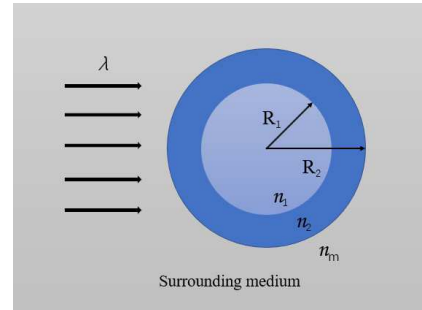


Fig. 2. Schematic of interaction between incident light and double-layer concentric spherical particle

Based on the Mie scattering theory, the light extinction, scattering, absorption cross-section, and absorption efficiency associated with the spherical particle can be calculated as follows:

$$C_{\text{ext}} = \frac{2\pi}{k^2} \sum_{n=1}^{\infty} (2n+1) \text{Re}(a_n + b_n) \quad (1) \quad C_{\text{sca}} = \frac{2\pi}{k^2} \sum_{n=1}^{\infty} (2n+1) (|a_n|^2 + |b_n|^2) \quad (2)$$

$$C_{\text{abs}} = C_{\text{ext}} - C_{\text{sca}} = \frac{2\pi}{k^2} \sum_{n=1}^{\infty} (2n+1) \left[\text{Re}(a_n + b_n) - |a_n|^2 - |b_n|^2 \right] \quad (3) \quad Q_{\text{ext}} = \frac{2}{x^2} \sum_{n=1}^{\infty} (2n+1) \text{Re}(a_n + b_n) \quad (4)$$

$$Q_{\text{sca}} = \frac{2}{x^2} \sum_{n=1}^{\infty} (2n+1) (|a_n|^2 + |b_n|^2) \quad (5)$$

$$Q_{\text{abs}} = Q_{\text{ext}} - Q_{\text{sca}} = \frac{2}{x^2} \sum_{n=1}^{\infty} (2n+1) \left[\text{Re}(a_n + b_n) - |a_n|^2 - |b_n|^2 \right] \quad (6)$$

Here, $k = 2\pi n_m / \lambda$ is the wave number of the incident wave in the surrounding medium, where n_m is the refractive index of the surrounding medium and λ is the wavelength of the incident light in vacuum; $x = kR$ represents the dimension parameter, where R is the radius of the particle; and a_n and b_n are both scattering coefficients expressed as follows:

$$a_n = \frac{m\psi_n(mx)\psi_n'(x) - \psi_n(x)\psi_n'(mx)}{m\psi_n(mx)\xi_n'(x) - \xi_n(x)\psi_n'(mx)} \quad (7) \quad b_n = \frac{\psi_n(mx)\psi_n'(x) - m\psi_n(x)\psi_n'(mx)}{\psi_n(mx)\xi_n'(x) - m\xi_n(x)\psi_n'(mx)} \quad (8)$$

Here, $m = n_p / n_m$ denotes the relative refractive index, where n_p is the refractive index of the spherical particle; $\psi_n(\rho) = \rho j_n(\rho)$ and $\xi_n(\rho) = \rho h_n^{(1)}(\rho)$ are the Riccati–Bessel functions of the first and third types, respectively, where $j_n(\rho)$ and $h_n^{(1)}(\rho)$ are the spherical Bessel functions of the first and third types, respectively. As indicated by these equations, when analysing the interaction between light and spherical particles based on the Mie scattering theory, the light distinction, scattering, and absorption characteristics associated with the spherical particle can be calculated directly and easily using the particular wavelength of the incident light, particle diameter, refractive index of the particle, and refractive index of the surrounding medium. a_n and b_n can be calculated using the numerical method described in the monograph by Bohren and Huffman [27].

2.2 Double-layer concentric spherical particle model

The light scattering and absorption characteristics of double-layer concentric spherical particles are often analysed based on the Mie scattering theory of double-layer concentric spheres [28]. The interaction between light and the double-layer concentric spherical particle is depicted in Fig. 2. As depicted in the figure, λ is the wavelength of the incident light; R_1 and R_2 are the radii of the core and shell, respectively; n_1 and n_2 are the refractive indices of the core and shell, respectively; and n_m is the refractive index of the surrounding medium.

The light distinction, scattering, absorption cross-section, and absorption efficiency associated with the double-layer concentric spherical particle can be calculated as follows:

$$C_{\text{ext}} = \frac{2\pi}{k^2} \sum_{n=1}^{\infty} (2n+1) \text{Re}(a_n'' + b_n'') \quad (9) \quad C_{\text{sca}} = \frac{2\pi}{k^2} \sum_{n=1}^{\infty} (2n+1) \left[|a_n''|^2 + |b_n''|^2 \right] \quad (10)$$

$$C_{\text{abs}} = C_{\text{ext}} - C_{\text{sca}} = \frac{2\pi}{k^2} \sum_{n=1}^{\infty} (2n+1) \left[\text{Re}(a_n'' + b_n'') - |a_n''|^2 - |b_n''|^2 \right] \quad (11)$$

$$Q_{\text{ext}} = \frac{2}{x_2} \sum_{n=1}^{\infty} (2n+1) \text{Re}(a_n'' + b_n'') \quad (12) \quad Q_{\text{sca}} = \frac{2}{x_2} \sum_{n=1}^{\infty} (2n+1) (|a_n''|^2 + |b_n''|^2) \quad (13)$$

$$Q_{\text{abs}} = Q_{\text{ext}} - Q_{\text{sca}} = \frac{2}{x_2} \sum_{n=1}^{\infty} (2n+1) \left[\text{Re}(a_n'' + b_n'') - |a_n''|^2 - |b_n''|^2 \right] \quad (14)$$

Here, $k = 2\pi n_m / \lambda$ represents the wave number of the incident wave in the surrounding medium, where n_m is the refractive index of the surrounding medium and λ is the wavelength of the incident light in vacuum; $x_2 = kR_2$ represents the dimension parameter, where R is the radius of the shell; and a_n'' and b_n'' are the scattering coefficients expressed as follows:

$$a_n'' = \frac{\psi_n(x_2) \left[\psi_n'(m_2 x_2) - A_n x_n'(m_2 x_2) \right] - m_2 \psi_n'(x_2) \left[\psi_n(m_2 x_2) - A_n x_n(m_2 x_2) \right]}{\xi_n(x_2) \left[\psi_n'(m_2 x_2) - A_n x_n'(m_2 x_2) \right] - m_2 \xi_n'(x_2) \left[\psi_n(m_2 x_2) - A_n x_n(m_2 x_2) \right]} \quad (15)$$

$$b_n'' = \frac{m_2 \psi_n(x_2) \left[\psi_n'(m_2 x_2) - B_n x_n'(m_2 x_2) \right] - \psi_n'(x_2) \left[\psi_n(m_2 x_2) - B_n x_n(m_2 x_2) \right]}{m_2 \xi_n(x_2) \left[\psi_n'(m_2 x_2) - B_n x_n'(m_2 x_2) \right] - \xi_n'(x_2) \left[\psi_n(m_2 x_2) - B_n x_n(m_2 x_2) \right]} \quad (16)$$

$$A_n = \frac{m_2 \psi_n(m_2 x_1) \psi_n'(m_1 x_1) - m_1 \psi_n'(m_2 x_1) \psi_n(m_1 x_1)}{m_2 x_n(m_2 x_1) \psi_n'(m_1 x_1) - m_1 x_n'(m_2 x_1) \psi_n(m_1 x_1)} \quad (17)$$

$$B_n = \frac{m_2 \psi_n(m_1 x_1) \psi_n'(m_2 x_1) - m_1 \psi_n'(m_1 x_1) \psi_n(m_2 x_1)}{m_2 x_n(m_2 x_1) \psi_n'(m_1 x_1) - m_1 x_n'(m_2 x_1) \psi_n(m_1 x_1)} \quad (18)$$

Here, m_1 and m_2 are the relative refractive indices of the core and shell, respectively; x_1 and x_2 are the dimension parameters of the core and shell, respectively; and ψ_n , x_n , and ξ_n are the Riccati–Bessel functions of the first, second, and third types, respectively. The expressions of these parameters are as follows:

$$m_1 = \frac{n_1}{n_m}, \quad m_2 = \frac{n_2}{n_m}, \quad x_1 = \frac{2\pi R_1 n_m}{\lambda}, \quad x_2 = \frac{2\pi R_2 n_m}{\lambda} \quad (19)$$

$$\psi_n(\rho) = \rho j_n(\rho), \quad x_n(\rho) = -\rho y_n(\rho), \quad \xi_n(\rho) = \rho h_n^{(1)}(\rho) \quad (20)$$

Here, n_1 and n_2 are the refractive indices of the core and shell, respectively; n_m is the refractive index of the surrounding medium; R_1 and R_2 are the radii of the core and shell, respectively; λ is the wavelength of the incident light in vacuum; and j_n , y_n , and h_n are spherical Bessel functions of the first, second, and third types, respectively. As expressed by these equations, the absorption characteristics of the particle can be analysed by numerical simulation using the wavelength of the incident light, radii of the core and shell, and refractive indices of the core, shell, and surrounding medium. a_n^I and b_n^I can be calculated using the numerical method described in the monograph by Bohren and Huffman [27]. The Mie theory allows Maxwell's equations to be solved when subjected to strict spherical boundary conditions. Although such a theory is only applicable to spherical particles, it is of significance for evaluating the accuracy of other approximation methods.

3 Characteristics of metallic nanoparticles

3.1 Surface Plasmon Resonance of the metallic nanoparticle

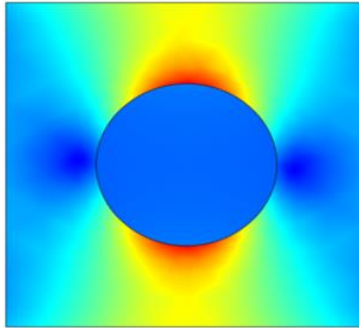


Fig. 3 electric field around single gold nanoparticle

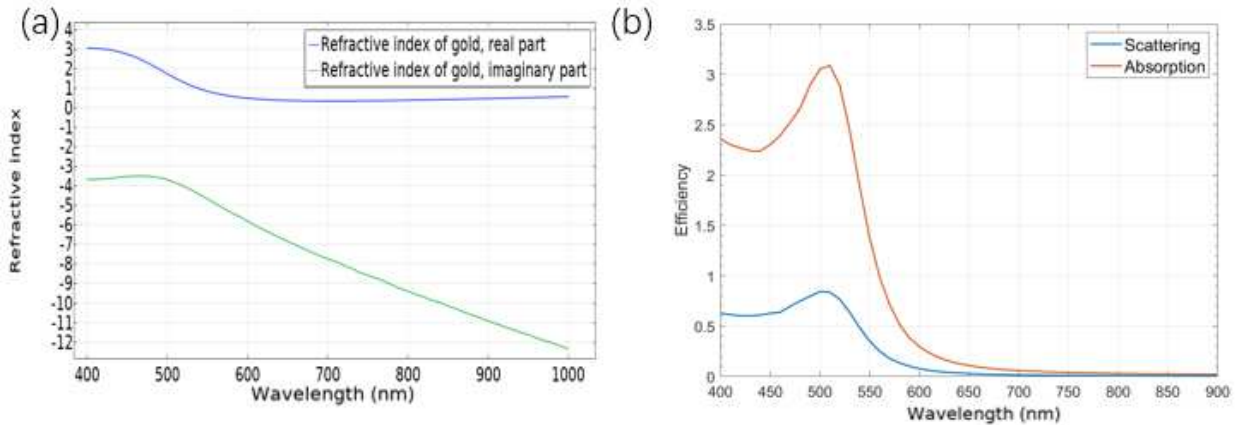


Fig. 4. (a) Refractive-index spectrum of gold nanoparticle; (b) scattering and absorption spectra of gold nanoparticle

When the localized Surface Plasmon Resonance (LSPR) of the metallic nanoparticle is excited by incident light, a strong absorption and scattering of the incident light occurs at the resonance wavelength of the metallic nanoparticle. In addition, the local electric field is enhanced significantly near the surfaces of the metal nanoparticles. Fig. 3 depicts the schematic of the electric field around a single gold nanoparticle. Fig. 4 (a) illustrates the variation in the refractive index of a gold nanoparticle. Fig. 4 (b) depicts the scattering and absorption spectra of the gold nanoparticle. It should be noted that the entire model is a sphere, while the scattering object is a metallic sphere. Owing to the symmetry of the spherical shape, only a hemisphere is used in our analysis. As can be seen from the results, the structure in our study shows a strong localization feature

3.2 Coupled structure of metallic nanoparticle with MIM waveguide

We design the schematic of a coupled structure comprising an MIM waveguide, rectangular split-ring resonator, and gold nanoparticle array. The grey, white, and yellow regions represent the metal (silver in this study), air, and gold nanoparticles, respectively. The height and width of the inner ring of the rectangular resonator are represented by h and w , respectively. The width of the gap located between the waveguides on both sides is represented by d . All the gold nanoparticles have a radius of 10 nm. To better describe the transmission characteristics of the waveguide structure, the transmittance of the waveguide is defined as the ratio of the output power P_{out} to the input power P_{in} , that is, $T = P_{\text{out}}/P_{\text{in}}$. Here, $P_{\text{in}} = \int P_{\text{oa}}vxdS_1$, $P_{\text{out}} = \int P_{\text{oa}}vxdS_2$, and $P_{\text{oa}}vxd$ is the x -axis component of the time-averaged power flow.

The dispersion relationship of transverse magnetic (TM) SPPs in the surface plasmonic MIM waveguide structure is expressed as follows [29]:

$$\tanh\left(\frac{d\sqrt{\beta^2 - k_0^2 \epsilon_{\text{in}}}}{2}\right) = \frac{-\epsilon_{\text{in}}\sqrt{\beta^2 - k_0^2 \epsilon_{\text{in}} \epsilon_{\text{m}}(\omega)}}{\epsilon_{\text{m}}(\omega)\sqrt{\beta^2 - k_0^2 \epsilon_{\text{in}}}} \quad (21)$$

Here, ϵ_{in} and ϵ_{m} are the dielectric constants of the medium and metal; $\beta = n_{\text{eff}}k_0$ is the complex propagation constant of SPPs; $k_0 = 2\pi/\lambda$ is the wave vector in vacuum, where λ is the wavelength of the incident light in vacuum; and n_{eff} is the effective refractive index of the mode. The dielectric constant of silver can be obtained using the Drude mode [30] as follows:

$$\epsilon_{\text{m}}(\omega) = \epsilon_{\infty} - \frac{\omega_p^2}{\omega^2 + i\omega\gamma} \quad (22)$$

where $\epsilon_{\infty} = 3.7$ is the dielectric constant at infinite angular frequency, $\omega_p = 9.1$ [eV] is the volume plasma frequency, $\gamma = 0.018$ [eV] is the collision frequency of electrons, and ω is the angular frequency of incident light.

4 Structural characteristics and sensing sensitivity analysis

4.1 Analysis of transmission characteristics

Fig.5 illustrates the transmission spectrum of coupled structures comprising a straight waveguide with a gap, rectangular split-ring resonator, and gold nanoparticle array. Fig.5 (b) and (d) depict a comparison of the transmission spectra between a single rectangular split-ring resonator and gold nanoparticle array. As depicted in Fig.5 (b), a narrow stopband occurs at 655 nm in the transmission spectrum of a single rectangular split-ring resonator owing to the weak coupling effect between the resonance cavity and the straight waveguide. This stopband can be considered as a narrow discrete state. Fig.5 (d) depicts the transmission spectrum generated through the coupling of the gold nanoparticle array and the straight waveguide. This spectrum represents a wide continuous state. Fig.5 (f) depicts the transmission spectrum generated by the coupled structure comprising both the rectangular split-ring resonator and the gold nanoparticle array. As depicted in the figure, there exist three transmission peaks at 610, 680, and 840 nm in the transmission spectrum. These peaks represent multiple resonance modes owing to the superposition of two discrete states and a continuous state. However, the peak transmittances do not reach 100% because of the internal loss inside the metal in the ring resonator and the slot waveguide. In particular, the transmission peak becomes weaker at a larger wavelength. This feature is attributed to the fact that the resonance generated with a long wavelength has a higher power than that with a short

wavelength. Such a finding indicates a promising prospect in the application of metal nanomaterials for plasma sensing. To better describe the mechanism of resonance generation, the distributions of the magnetic fields associated with the three wavelengths depicted in Fig.5 (b), (d), and (f) are illustrated in Fig.5 (a), (c), and (e), respectively.

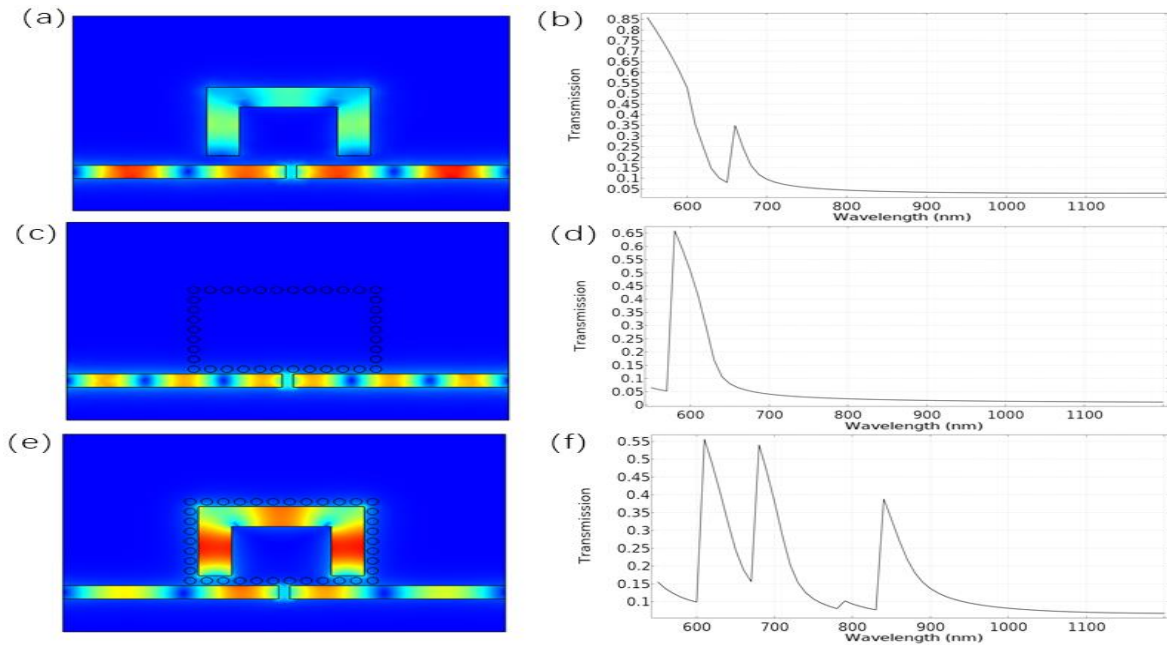


Fig.5. Distribution of magnetic field associated with (a) single rectangular split-ring resonator, (c) gold nanoparticle array, (e) rectangular split-ring resonator coupled with gold nanoparticle array. (b), (d), and (f) depict the transmission spectra corresponding to the magnetic fields depicted in (a), (c), and (e).

4.2 Relationship between full width at half maximum of transmission and resonance spectra

In the previous section, we analysed the effect of the geometric parameters of the proposed structure on the resonance spectrum. Fig.6 depicts the relationship between the full width at half maximum (FWHM) of the transmission and the resonance spectra when the internal width w of the rectangular split-ring resonator is increased from 160 to 200 nm. The resolution of the sensor, that is, the smallest change in the refractive index of the sample that can be detected by the sensing system, is expressed by the FWHM. As depicted in Fig.6 (a), increasing the width w with other parameters fixed ($d = 20$ nm, $h = 120$ nm) leads to a red-shift in the resonance spectrum. In addition, the transmittances of modes 1, 2, and 3 are increased from 0.43 to 0.67, 0.61 to 0.46, and 0.26 to 0.5, respectively. Fig.6 (b) depicts the variation in the FWHM of the resonance spectrum as the internal width of the rectangular split-ring is increased from 160 to 200 nm. As indicated in the figure, the FWHMs of modes 1, 2, and 3 are increased from 34 to 47 nm, increased from 44 to 33 nm, and first decreased from 48 to 42 nm and then increased to 51 nm, respectively. Based on the transmittance and FWHM results, the appropriate value of the coupling distance parameter w is selected as 180 nm.

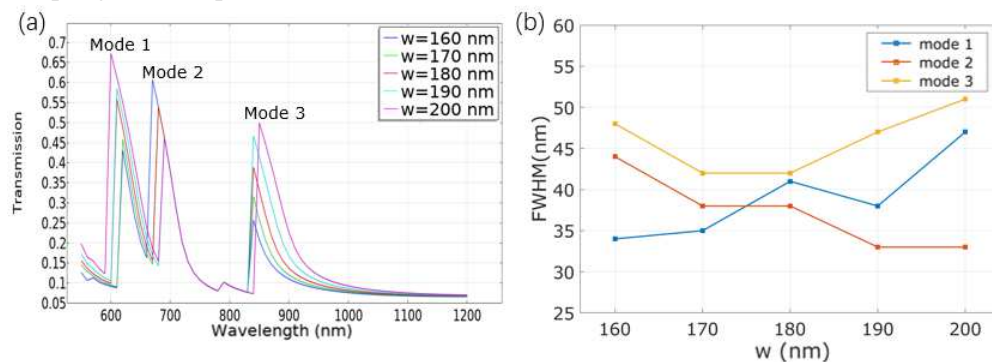


Fig. 6(a) Transmission spectrum obtained by increasing internal width w of rectangular split-ring from 160 to 200 nm; (b) relationship between width w and FWHM of resonance spectrum

Next, we analysed the effect of the internal height of the rectangular split-ring on the transmission spectrum by increasing h from 160 to 200 nm but maintaining other parameters constant ($d = 20$ nm, $w = 180$ nm). As depicted in Fig.7(a), increasing the height h results in a red-shift in the resonance spectrum. In addition, the transmittances of modes 1, 2, and 3 are increased from 0.24 to 0.7, decreased from 0.61 to 0.47, and first increased from 0.35 to 0.39 and then decreased to 0.35, respectively. Fig.7(b) depicts the variation in the FWHM of the resonance spectrum as the internal height of the rectangular split-ring is increased from 160 to 200 nm. As indicated in the Fig., the FWHMs of modes 1, 2, and 3 are first decreased from 43 to 33 nm and then increased to 50 nm, decreased from 44 to 35 nm, and remains relatively stable at approximately 42 nm, respectively. Based on the transmittance and FWHM results, the appropriate value of the coupling distance parameter h is selected as 148 nm.

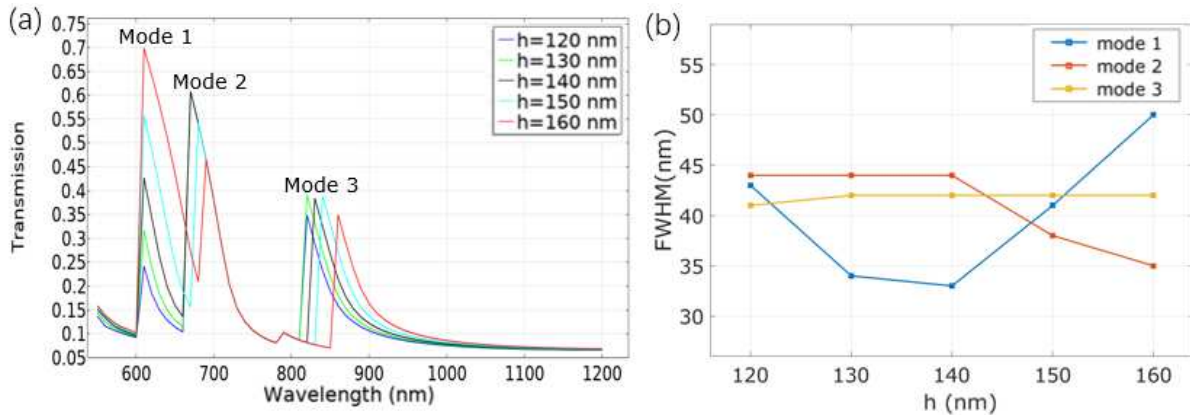


Fig.7 (a) Transmission spectrum obtained by increasing internal height h of rectangular split-ring from 120 to 160 nm; (b) relationship between height h and FWHM of resonance spectrum.

Finally, we analysed how the transmission spectrum is affected by increasing the width d of the gap between the two waveguides from 20 to 40 nm while maintaining other parameters constant ($h = 148$ nm, $w = 180$ nm). As depicted in Fig.8(a), an increasing gap width d leads to a blue-shift in the resonance spectrum. In addition, the transmittances of modes 1, 2, and 3 are increased slightly from 0.55 to 0.62, decreased from 0.52 to 0.4, and increased from 0.38 to 0.54, respectively. Fig.8(b) depicts the variation in the FWHM of the resonance spectrum as the gap width d is increased from 20 to 40 nm. As illustrated in the Fig.8, the FWHMs of modes 1 are increased from 41 to 47 nm, decreased from 38 to 30 nm, and increased from 42 to 56 nm, respectively. Based on the transmittance and FWHM results, the appropriate value of the coupling distance parameter d is selected as 20 nm.

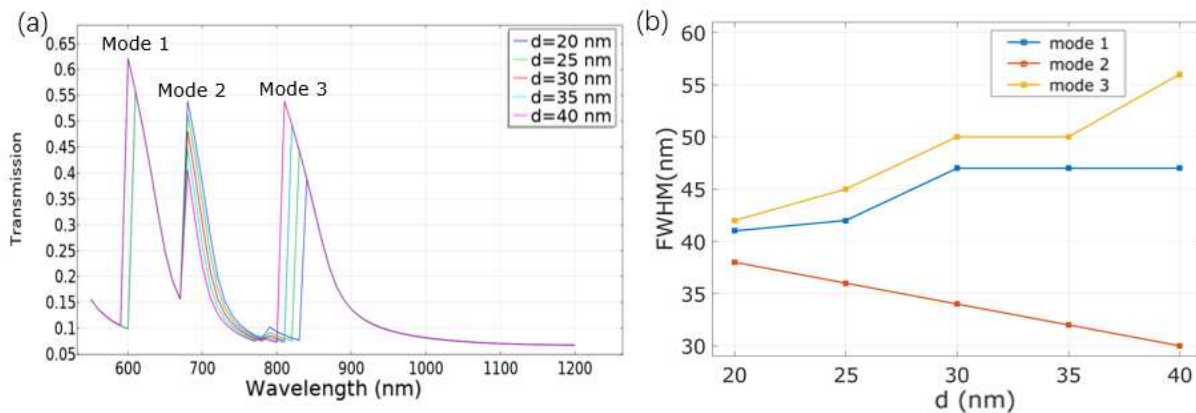


Fig.8. (a) Transmission spectrum obtained with gap width d between two waveguides increasing from 20 to 40 nm; (b) relationship between gap width d and FWHM of resonance spectrum.

4.3 Sensitivity analysis of refractive index

Based on the analyses of the structural parameters discussed above, two significant performance parameters are introduced to evaluate the refractive index of the sensor at the nanoscale. These two parameters are the sensitivity S and the FOM. The sensitivity is defined as follows:

$$S = \Delta\lambda/\Delta n \text{ (nm/RIU)} \quad (23)$$

which represents the resonance spectral shift associated with each refractive index unit. FOM is defined as follows:

$$\text{FOM} = \frac{S}{\text{FWHM}} \quad (24)$$

which offers a good means to evaluate the performance of the sensor. Fig. 9 depicts the transmission spectrum when the refractive index of the filling medium in the structure is increased from 1 to 1.02 as other parameters are maintained constant ($h = 148$ nm, $w = 180$ nm, and $d = 20$ nm). It is evident that increasing the refractive index n leads to a substantial red-shift in the resonance spectrum. Specifically, as n is increased from 1 to 1.02, the resonance spectrum is shifted by 10 nm at mode 1 and by 20 nm at modes 2 and 3. Fig. 9(b) depicts the variation in the FWHM as the refractive index of the filling material is increased from 1 to 1.02. Using equation (23), the refractive index sensitivities of modes 1, 2, and 3 are calculated as 500, 1000, and 1000 nm/RIU, respectively. Using equation (24), the FOMs of modes 1, 2, and 3 are calculated as 12, 27.7, and 23.8, respectively. These results suggest that the proposed structure exhibits a high refractive index sensitivity and a large FOM value. In other words, the proposed structure exhibits an excellent refractive index sensing property. These research findings have opened up new paths in the design and optimisation of nanoscale refractive index sensors.

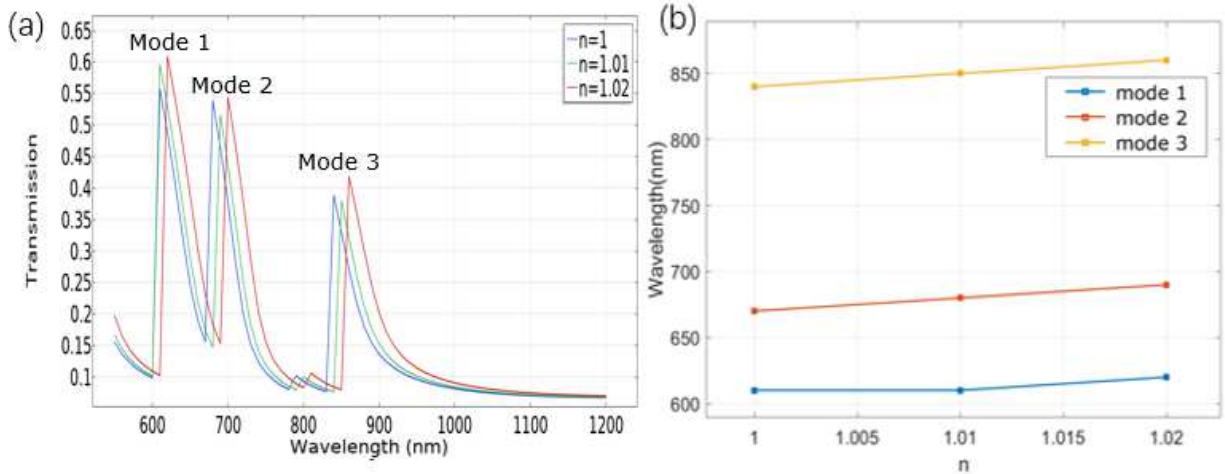


Fig. 9. (a) Transmission spectrum obtained with refractive index of medium increasing from 1 to 1.02; (b) variation in resonance wavelength with respect to refractive index n .

5. Conclusion

In this study, a plasmonic refractive index sensor based on the metallic nanoparticle-coupled MIM waveguide structure was designed and analysed. The sensitivity and FOM of the proposed structure could be optimised easily by adjusting the size of the structure. The proposed device exhibited high sensitivity and a small volume, making it suitable for system integration. The FWHMs of modes are increased from 41 to 47 nm, decreased from 38 to 30 nm, and increased from 42 to 56 nm, respectively. Based on the transmittance and FWHM results, the appropriate value of the coupling distance parameter d is selected as 20 nm. By filling the test area with a medium possessing different refractive indices, a refractive index sensor at nanometre scale could be

developed with a sensitivity of up to 1000 nm/RIU and an FOM of 23.8. Thus, the proposed structure holds significant potential for on-chip optical sensing applications.

Declarations

*Funding: This project is supported by National Natural Science Foundation of China (Grant No. 51965007) , "One thousand Young and Middle-Aged College and University Backbone Teachers Cultivation Program" of Guangxi(2019), Guangxi Natural Science Foundation.

*Conflicts of interest/Competing interests: No conflict of interest exists in the submission of this manuscript

*Availability of data and material: All data generated or analysed during this study are included in this article

*Code availability: We ensure availability of supporting data

*Authors' contributions: Yihong Ren and JUN ZHU drafted the manuscript. All authors read and approved the final manuscript.

*Ethics approval: The experiments of our paper have no ethical issues. And the experimental protocols were approved by the Animal Care and Protection Committee of Guangxi Normal University.

*Consent to participate: Written informed consent was obtained from all the authors for publication of their individual details and accompanying images in this manuscript.

References:

- [1] Mehmet Kahraman, Pallavi Daggumati, Ozge Kurtulus, Erkin Seker, Sebastian Wachsmann-Hogiu. Fabrication and Characterization of Flexible and Tunable Plasmonic Nanostructures[J]. Scientific Reports, 2013, 3(1).
- [2] Chen Wei Ting, Wu Pin Chieh, Chen Chen Jung, Chung Hung-Yi, Chau Yuan-Fong, Kuan Chieh-Hsiung, Tsai Din Ping. Electromagnetic energy vortex associated with sub-wavelength plasmonic Taiji marks[J]. Optics express, 2010, 18(19).
- [3] Maier S A, Atwater H A. Plasmonics: Localization and guiding of electromagnetic energy in metal/dielectric structures[J]. Journal of Applied Physics, 2005, 98(1): 011101.
- [4] Chih-Chan Hu, Wayne Yang, Yao-Tsung Tsai, Yuan-Fong Chau. Gap enhancement and transmittance spectra of a periodic bowtie nanoantenna array buried in a silica substrate[J]. 2014(324).
- [5] Yuan-Fong Chau, Zheng-Hong Jiang. Plasmonics Effects of Nanometal Embedded in a Dielectric Substrate[J]. Plasmonics, 2011, 6(3).
- [6] Sung Ming-Je, Ma Yao-Feng, Chau Yuan-Fong, Huang Ding-Wei. Surface plasmon resonance in a hexagonal nanostructure formed by seven core shell nanocylinders[J]. Applied optics, 2010, 49(5).
- [7] Park Junghyun, Kim Hwi, Lee Byoung-ho. High order plasmonic Bragg reflection in the metal-insulator-metal waveguide Bragg grating[J]. Optics express, 2008, 16(1).
- [8] Yuan-Fong Chou Chau, Chung-Ting Chou Chao, Hung Ji Huang, N. T. R. N. Kumara, Chee Ming Lim, Hai-Pang Chiang. Ultra-High Refractive Index Sensing Structure Based on a Metal-Insulator-Metal Waveguide-Coupled T-Shape Cavity with Metal Nanorod Defects[J]. Nanomaterials, 2019, 9(10).
- [9] Zhang Cong, Bai Ruiping, Gu Xintong, Jin Xing Ri, Zhang Ying Qiao, Lee Young Pak. Dual-band unidirectional reflectionless phenomena in an ultracompact non-Hermitian plasmonic waveguide system based on near-field coupling [J]. Optics express, 2017, 25(20).
- [10] Chau Y F C. Mid-infrared sensing properties of a plasmonic metal-insulator-metal waveguide with a single stub including the defects[J]. Journal of Physics D Applied Physics, 2019, 53(11).
- [11] Neo Yoichiro, Matsumoto Takahiro, Watanabe Takeshi, Tomita Makoto, Mimura Hidenori. Transformation from plasmon-induced transparency to -induced absorption through the control of coupling strength in metal-insulator-metal structure [J]. Optics express, 2016, 24(23).
- [12] Wang Guoxi, Lu Hua, Liu Xueming, Gong Yongkang, Wang Leiran. Optical bistability in metal-insulator-metal plasmonic waveguide with nanodisk resonator containing Kerr nonlinear medium [J]. Applied optics, 2011, 50(27).
- [13] Xiao Li-Ping, Wang Fa-Qiang, Liang Rui-Sheng, Zou Shi-Wei, Hu Miao. A High-Sensitivity Refractive-Index Sensor Based on Plasmonic Waveguides Asymmetrically Coupled with a Nanodisk Resonator Supported by the National Natural Science Foundation of China under Grant No 61275059 [J]. Chinese Physics Letters, 2015, 32(7).
- [14] Wu Tiesheng, Liu Yumin, Yu Zhongyuan, Peng Yiwei, Shu Changgan, Ye Han. The sensing characteristics of plasmonic waveguide with a ring resonator [J]. Optics express, 2014, 22(7).
- [15] Min Changjun, Wang Pei, Jiao Xiaojin, Deng Yan, Ming Hai. Beam manipulating by metallic nano-optic lens containing nonlinear media [J]. Optics express, 2007, 15(15).
- [16] Lu Hua, Liu Xueming, Mao Dong, Wang Leiran, Gong Yongkang. Tunable band-pass plasmonic waveguide filters with nanodisk resonators[J]. Optics express, 2010, 18(17).
- [17] Shen L, Yang T J, Chau Y F. Effect of internal period on the optical dispersion of indefinite-medium materials[J]. Physical Review B, 2008, 77(20).
- [18] Lu Hua, Liu Xueming, Mao Dong, Wang Guoxi. Plasmonic nanosensor based on Fano resonance in waveguide-coupled resonators[J]. Optics letters, 2012, 37(18).
- [19] Zheng G, Chen Y, Xu L, M Lai, Y Liu. Metal-insulator-metal waveguide-based band-pass filter with circular ring resonator containing Kerr nonlinear medium[J]. Optics Communications, 2013, 305(Complete).
- [20] Hua Lu, GuoXi Wang, XueMing Liu. Manipulation of light in MIM plasmonic waveguide systems[J]. Chinese Science Bulletin, 2013, 58(30).
- [21] Zhaojian Zhang, Junbo Yang, Xin He, Jingjing Zhang, Jie Huang, Dingbo Chen, Yunxin Han. Plasmonic Refractive Index Sensor with High Figure of Merit Based on Concentric-Rings Resonator[J]. Sensors, 2018, 18(1).

- [22] Yunping Qi, Peiyang Zhou, Ting Zhang, Xuewei Zhang, Yue Wang, Chuqin Liu, Yulong Bai, Xiangxian Wang. Theoretical study of a multichannel plasmonic waveguide notch filter with double-sided nanodisk and two slot cavities[J]. Results in Physics,2019,14.
- [23] Zicong Guo, Kunhua Wen, Qinyang Hu, Wenhui Lai, Jiyan Lin, Yihong Fang. Plasmonic Multichannel Refractive Index Sensor Based on Subwavelength Tangent-Ring Metal–Insulator–Metal Waveguide[J]. Sensors, 2018, 18(5).
- [24] K. R. Kishore, Singh Utkarsh, N. Ayyanar, G. Thavasi Raja, M. S. Sanathanan. Hybrid plasmonic label-free multi-analyte refractive index sensor[J]. Optoelectronics Letters, 2019, 15(4).
- [25] Mie G. Beiträge zur Optik trüber Medien, speziell kolloidaler Metallösungen[J]. Ann Phys,1908, 25.
- [26] Kerker M. The Scattering of Light and Other Electromagnetic Radiation[M]. New York: Academic Press, 1969.
- [27] Bohren C F, Huffman D R. Absorption and Scattering of Light by Small Particles[M]. New York: John Wiley & Sons, 1983.
- [28] Aden A L, Kerker M. Scattering of electromagnetic waves from two concentric spheres[J]. JAppl Phys, 1951, 22.
- [29] Kim Ki Young, Cho Young Ki, Tae Heung-Sik, Lee Jeong-Hae. Light transmission along dispersive plasmonic gap and its subwavelength guidance characteristics[J]. Optics express, 2006, 14(1).
- [30] Chen Lei, Liu Yumin, Yu Zhongyuan, Wu Dong, Ma Rui, Zhang Yang, Ye Han. Numerical analysis of a near-infrared plasmonic refractive index sensor with high figure of merit based on a fillet cavity[J]. Optics express, 2016, 24(9).

Figures

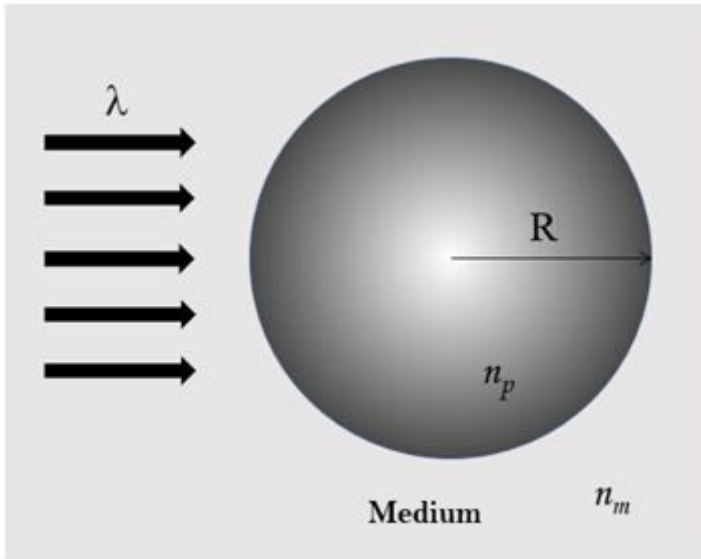


Figure 1

Schematic of mutual interaction between incident light and single-layer spherical article

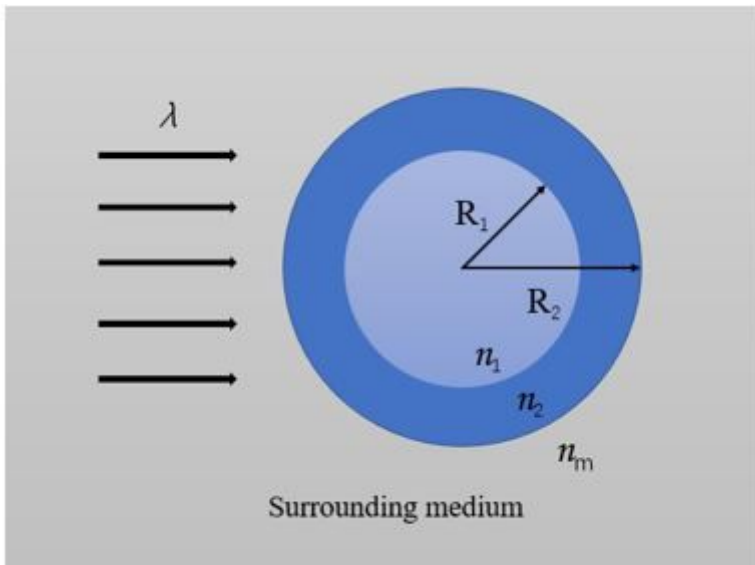


Figure 2

Schematic of interaction between incident light and double-layer concentric spherical particle

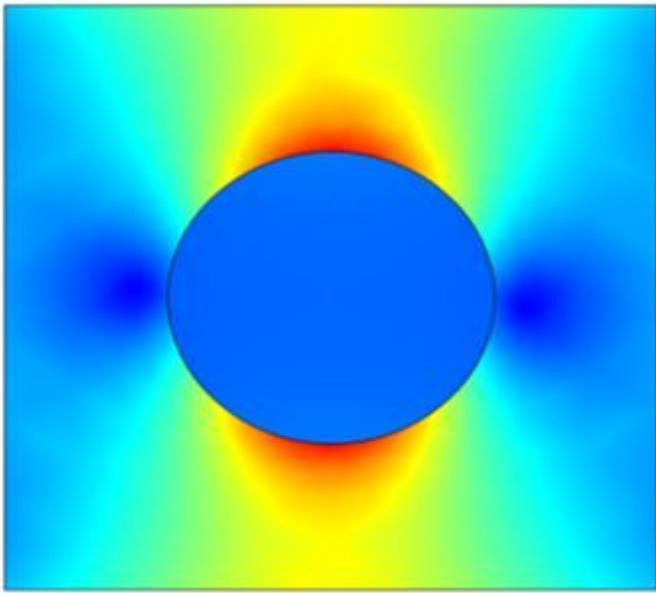


Figure 3

electric field around single gold nanoparticle

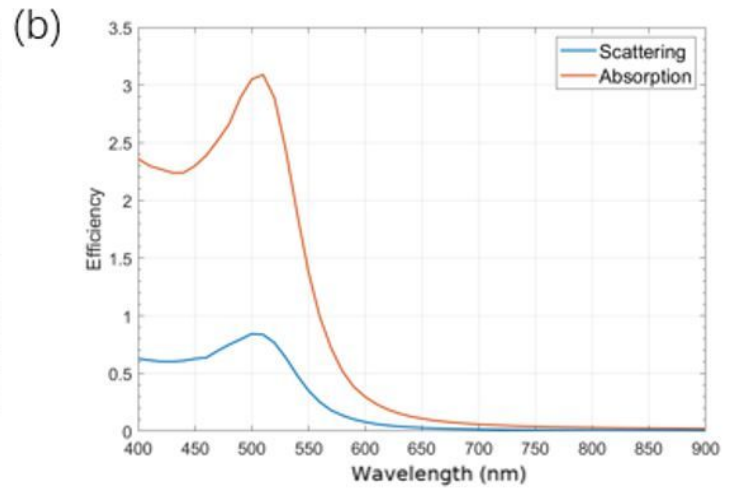
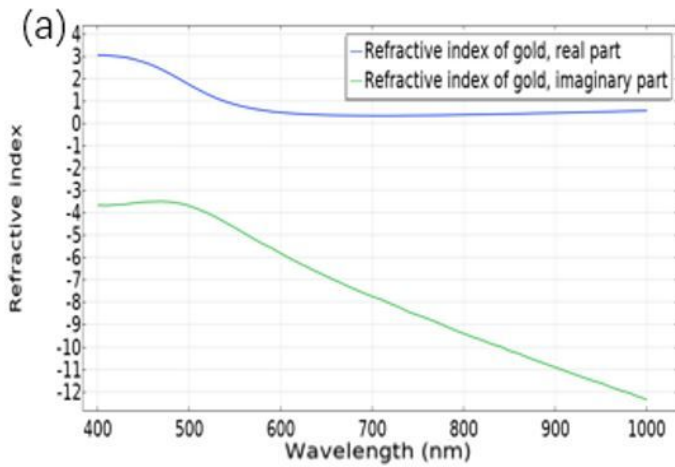


Figure 4

(a) Refractive-index spectrum of gold nanoparticle; (b) scattering and absorption spectra of gold nanoparticle

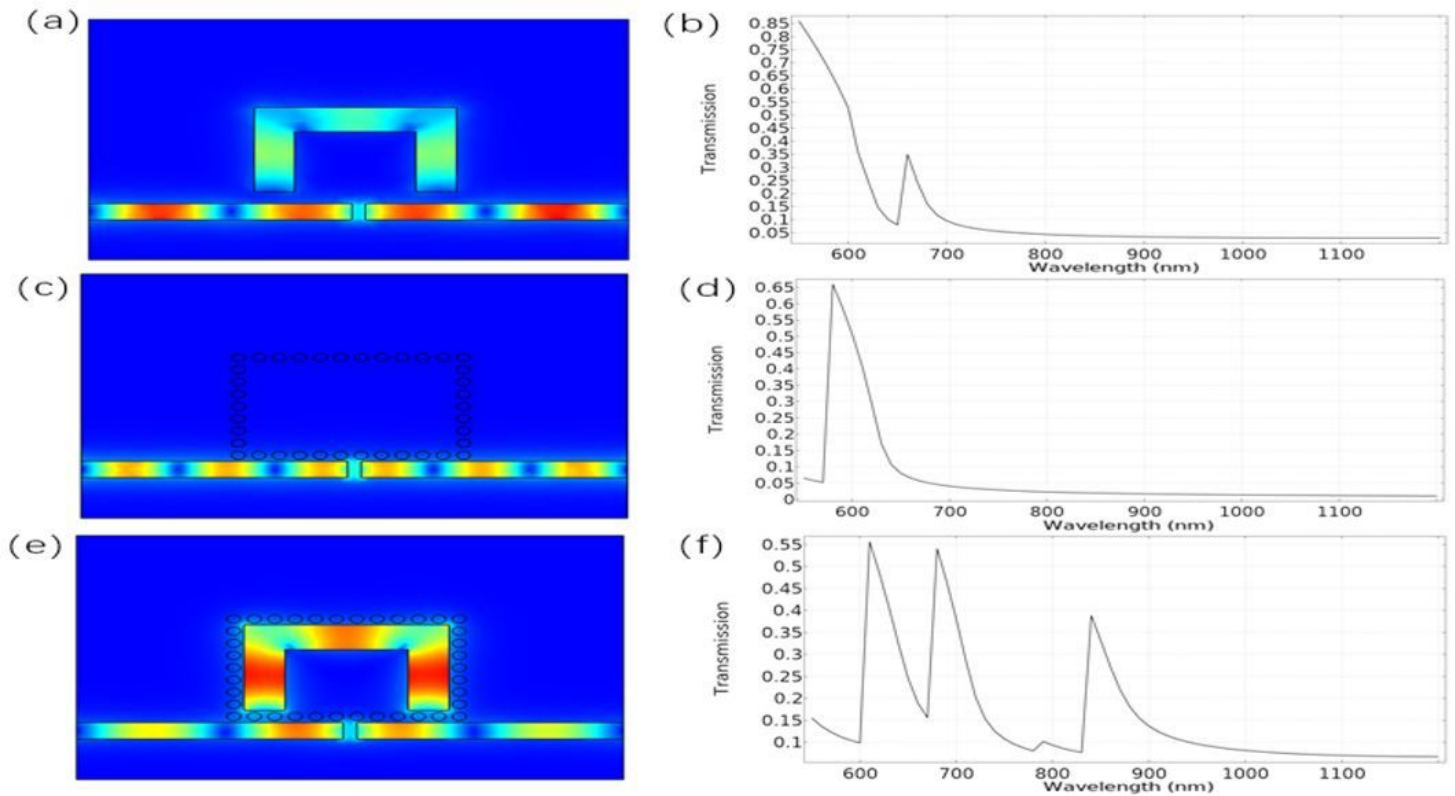


Figure 5

Distribution of magnetic field associated with (a) single rectangular split-ring resonator, (c) gold nanoparticle array, (e) rectangular split-ring resonator coupled with gold nanoparticle array. (b), (d), and (f) depict the transmission spectra corresponding to the magnetic fields depicted in (a), (c), and (e).

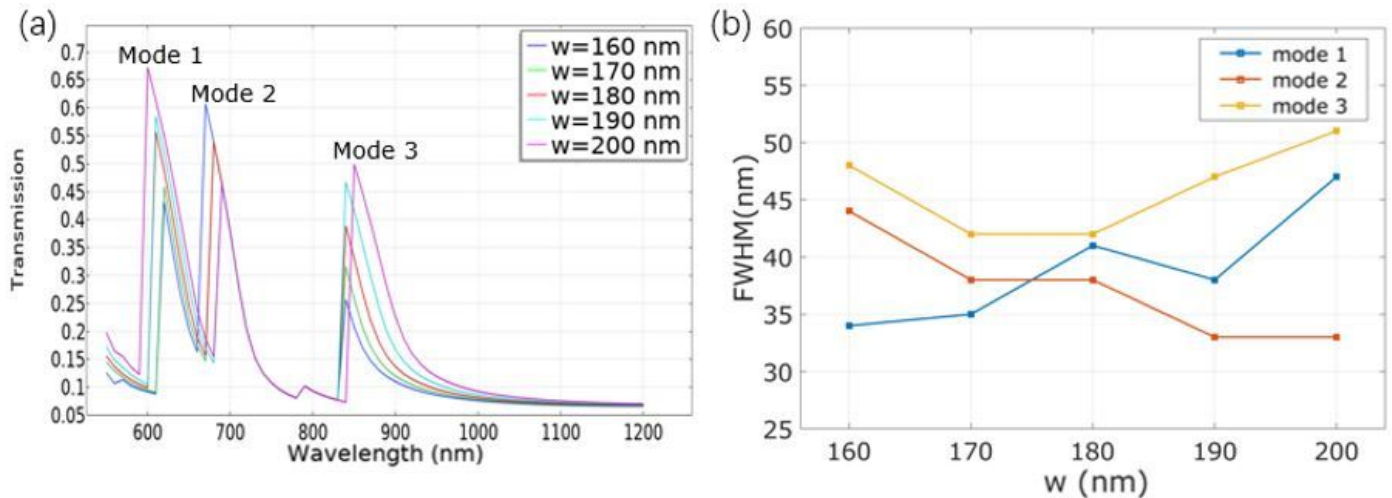


Figure 6

(a) Transmission spectrum obtained by increasing internal width w of rectangular split-ring from 160 to 200 nm; (b) relationship between width w and FWHM of resonance spectrum

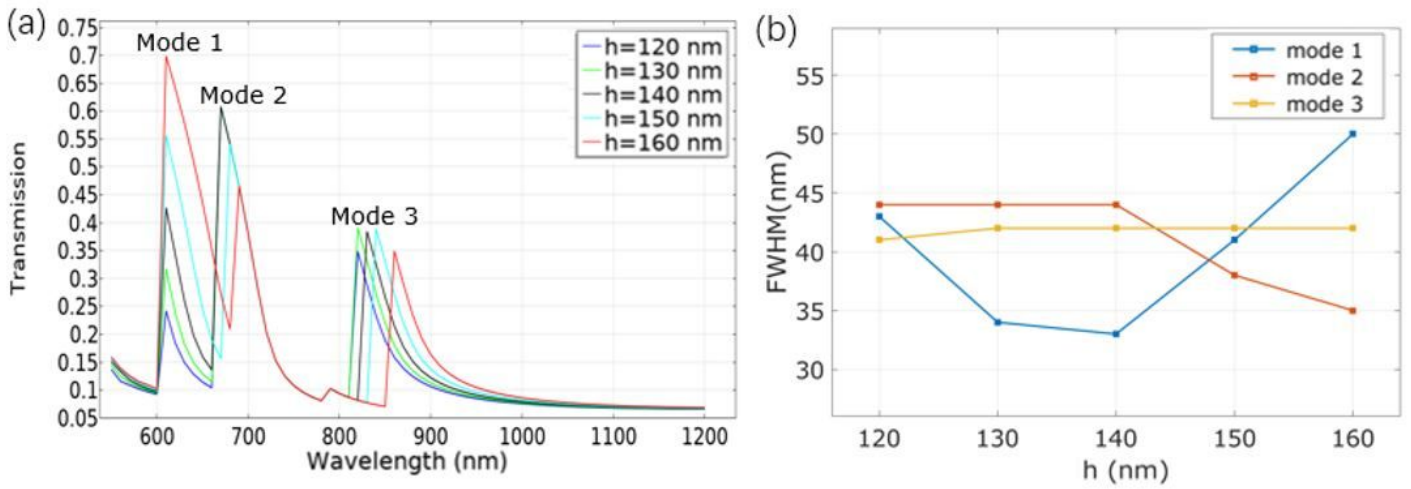


Figure 7

(a) Transmission spectrum obtained by increasing internal height h of rectangular split-ring from 120 to 160 nm; (b) relationship between height h and FWHM of resonance spectrum.

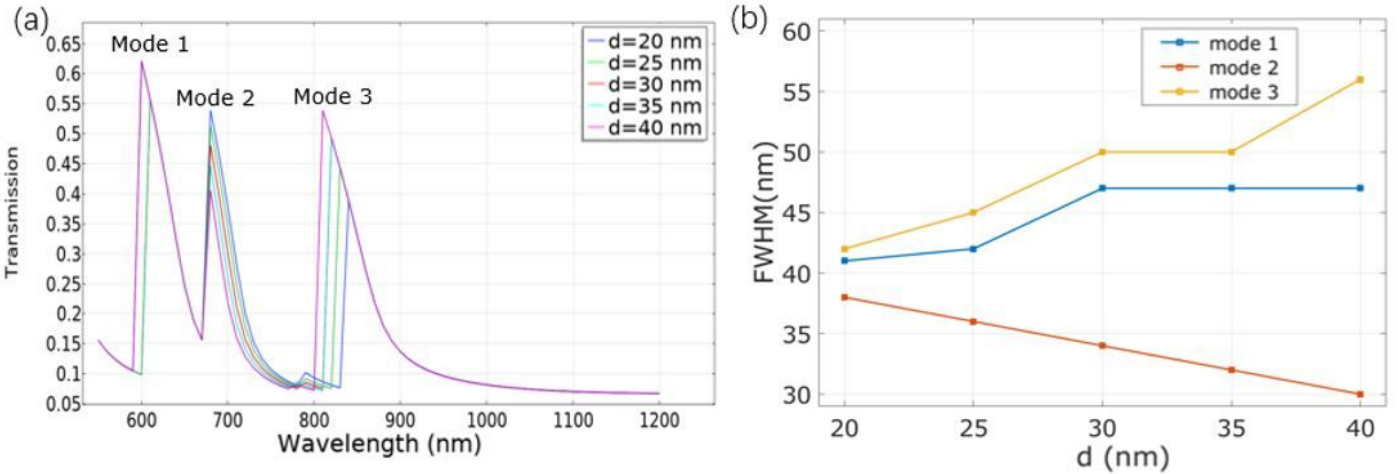


Figure 8

(a) Transmission spectrum obtained with gap width d between two waveguides increasing from 20 to 40 nm; (b) relationship between gap width d and FWHM of resonance spectrum.

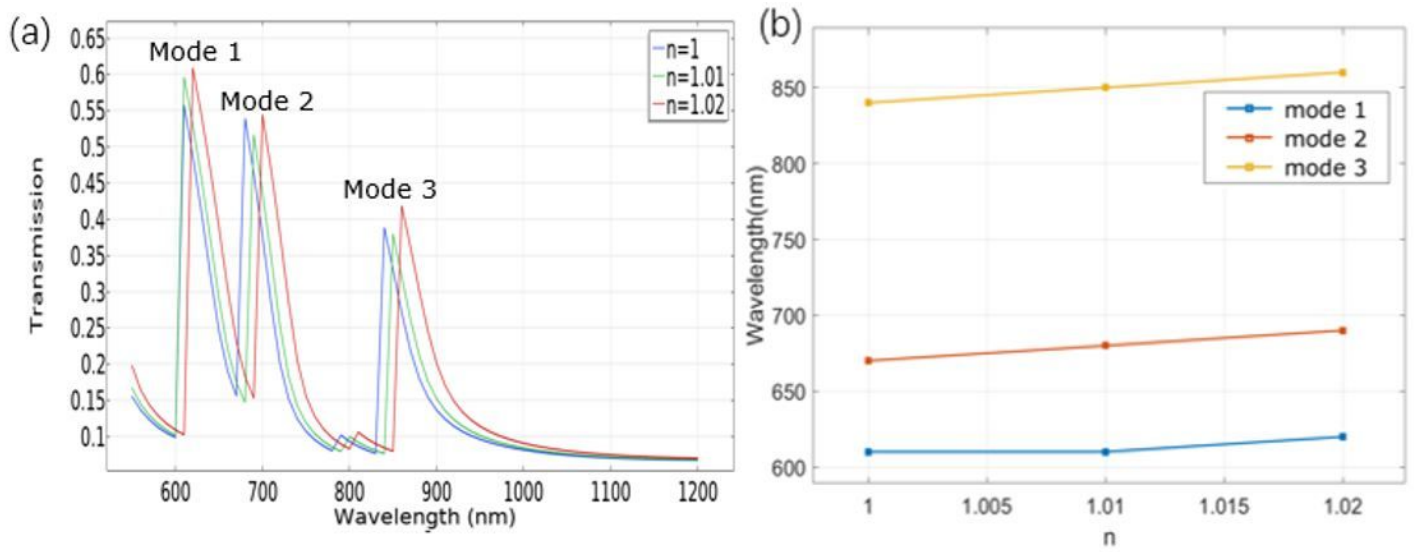


Figure 9

(a) Transmission spectrum obtained with refractive index of medium increasing from 1 to 1.02; (b) variation in resonance wavelength with respect to refractive index n .